Nanoscale

Accepted Manuscript

This article can be cited before page numbers have been issued, to do this please use: L. A. Alvarado Leal, J. I. Paez Ornelas, M. Ruiz, J. Guerrero-Sanchez, J. M. Romo-Herrera, N. Fernandez-Escamilla, N. Takeuchi and E. Perez-Tijerina, *Nanoscale*, 2024, DOI: 10.1039/D4NR02713B.

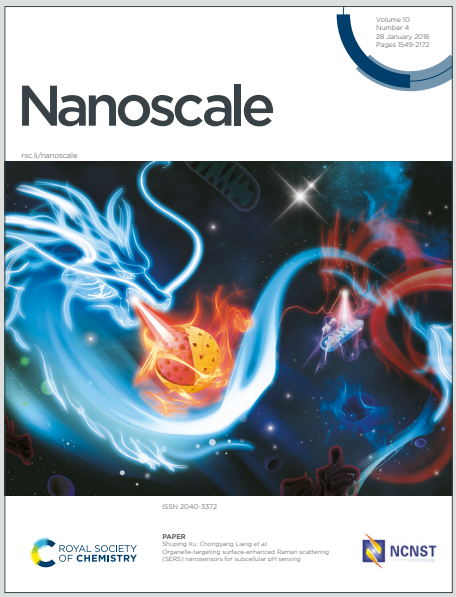

ROYAL SOCIETY OF CHEMISTRY

rsc.li/nanoscale

View Article Online
DOI: 10.1039/D4NR02713B

Exploring Nitrogen-Mediated Effects on Fe and Cu Cluster Development in Graphene: A DFT Study.

L. A. Alvarado-Leal[1] ∗, J. I. Páez-Ornelas[2], M. A. Ruiz-Robles[1], J. Guerrero-Sánchez[2], J. M. Romo-Herrera [2], H. N. Fernández-Escamilla[1], Noboru Takeuchi[2], E.G. Perez-Tijerina [1]

[1] CICFIM Facultad de Ciencias Físico Matemáticas, Universidad Autónoma de Nuevo León, San Nicolás de los Garza, Nuevo León, Código Postal 66450, México.
[2] Centro de Nanociencias y Nanotecnología, Universidad Nacional Autónoma de México, Apartado Postal 14, Ensenada Baja California, Código Postal 22800, México.

AUTHOR INFORMATION
Corresponding author
∗**E-mail: luis.alvaradoll@uanl.edu.mx**

Abstract:

The controlled growth and stability of transition metal clusters on N-doped materials have become the subject of intense investigation for unveiling comprehension on the cluster growth evolution. In this study, we investigated the growth mechanisms of non-magnetic (copper) and magnetic (iron) clusters on graphene with two atomic vacancies, with and without pyridinic nitrogen (N). Our results determine the role of pyridinic N in the growth, and physicochemical properties of the mentioned metal clusters. In an N environment, Cu grows perpendicularly, whereas in N-deficient conditions, the cluster agglomerates. The Fe cumulate-type clusters are formed regardless of the presence of N. However, N causes the Fe cluster to rise over one side of the surface without deforming the monolayer; meanwhile, in the absence of N, the Fe cluster protrudes from both sides of the monolayer. Remarkably, the N presence makes feasible to induce magnetization in the Cu_n–N_4V_2 systems and aid focalizing the magnetic properties on the Fe cluster for the Fe_n–N_4V_2 case. These findings offer insights into the role of N in cluster growth, with potential implications for diverse applications, including magnetic and electrocatalytic materials.

KEYWORDS: Graphene, DFT, Clusters, Transition Metal Adatoms

View Article Online
DOI: 10.1039/D4NR02713B

1 Introduction.

In recent years, the integration of graphene and transition metals has emerged as a promising route in materials science, offering unique opportunities for tailoring electronic, magnetic, and catalytic properties at the nanoscale [1, 2]. In particular, the controlled growth and stability of transition metal clusters on graphene surfaces have become the subject of intense investigation [3, 4].

Recent studies have demonstrated that when small groups of Ni, Pd, and Pt atoms are adsorbed on a graphene layer, they generally retain the structural characteristics of gas-phase atomic groups [5, 6]. However, the strength of their interaction weakens as the size of the metal groups increases [5–8]. Moreover, researchers have explored the adsorption of transition metal atoms on graphene to modify their electronic, magnetic, and surface reactivity properties. This exploration holds significant implications in diverse fields, including spintronics, nanomagnetism, data storage, and catalysis [9–12].

Parallel investigations have scrutinized the interactions between metal clusters and graphene sheets, revealing that interfacial energy substantially influences the stability of these metal/graphene systems [13]. Similar interaction energies are observed for specific cluster sizes, even when oriented differently upon contact with the graphene material [13]. Another research strand is the potential of employing diverse defective graphene sheets to support transition metals [14]. It was observed that metals form stronger bonds with defective graphene, thereby contributing to their stabilization without significantly compromising the magnetic properties. Notably, magnetic anisotropy is boosted substantially when certain metals are deposited on defective graphene despite the intrinsic non-magnetic nature of carbon [15, 16].

Recent density functional theory studies have advanced our understanding of the structural, electronic, and magnetic properties of small transition metal clusters. For iron clusters (Fe_n, $n \leq 17$), significant findings include “magic numbers" at specific sizes ($n = 6$, 8, 10, 13, and 15) and non-collinear magnetic structures influenced by the Jahn-Teller effect, revealing high magnetic moments across varying configurations. The chemical reactivity of these clusters is primarily influenced by the coordination of individual atoms, and the addition of cobalt (Co) has been shown to enhance magnetic properties through structural rearrangements, providing insights into potential catalytic and magnetic applications [17–20]. Additionally, studies on small copper clusters (Cu_n, $n \leq 15$) have demonstrated a preference for compact structures and identified unique growth pathways such as triangular and pentagonal bipyramidal arrangements. Furthermore, copper clusters on graphene quantum dots (GQDs) exhibit enhanced binding energy and conductivity, particularly when vacancies are present in the graphene, highlighting new strategies for catalytic applications [21, 22].

Multiple variables, including the chemical environment, can impact the incorporation or growth of metals on the graphene network. These variables must be carefully analyzed to determine the factors that could favor or disfavor the process to obtain the desired metal/graphene system. Whether by cluster aggregation or growth, from the design of a single-atom catalyst (SAC) to a specific (few atoms) cluster, the process must be controllable and reproducible.

The performance of metallic SACs can be adversely affected by a considerable increase in the size of metal clusters and increased surface roughness, leading to a decrease in efficiency [23–25]. The primary objectives when trying to synthesize metallic SACs are high dispersion of individual atoms on suitable supports, i.e., graphitic surfaces [26–29], and reduction of contamination due to byproducts during synthesis. The most reasonable option to conduct experimental investigations on metallic

View Article Online
DOI: 10.1039/D4NR02713B

SACs is the vacuum deposition method due to its good control over cluster size [30, 31] and non-byproduct formation during synthesis. Therefore, this is a great opportunity for synthesis methods employing mass-selected and soft-landing techniques [32–35] in combination with magnetron sputtering [36] or inert gas condensation [37–39] due to their high atomic dispersion on substrates [40], highly controlled cluster size [41, 42], and exceptionally low contamination compared with chemical methods that utilize molecules as stabilizers and chemical reactants as precursors of metallic atoms [43], such as iron (Fe) single atoms and clusters [44–48].

The incorporation of nitrogen into the carbon lattice has been widely explored for many reasons, such as modifying graphene's electronic properties and enabling fine-tuning of its electrical conductivity [49, 50]. It is reported that nitrogen stabilizes carbon lattices with atomic vacancies or structural deformations. N-doped systems, such as N-doped nanotubes, are also widely applied in catalytic reactions [51, 52]. Furthermore, nitrogen can facilitate strong interactions with transition metal atoms, potentially influencing cluster nucleation and growth [53, 54]. Recent studies have shown that N-doped graphene-supported clusters, such as $Fe_3@N_4C_{16}$, exhibit enhanced electrocatalytic performance in the electrochemical nitrogen reduction reaction (eNRR) due to the modulation of the local electronic environment by nitrogen coordination [55].

Transition metal single-atom catalysts (SACs) and clusters supported on graphene have demonstrated exceptional catalytic activity in various chemical reactions, and the ability to control their formation and stability through nitrogen doping can open new avenues for designing efficient catalysts [56–58]. In this study, we employed density functional theory (DFT) calculations to explore the effects of nitrogen on the formation and stability of magnetic and non-magnetic clusters (Fe and Cu, respectively) on graphene substrates. Specifically, we investigated the cluster aggregation and growth mechanisms from one to six-atom clusters at carbon vacancies with and without pyridinic nitrogen, shedding light on the underlying mechanisms and potential applications of these composite systems. The outcomes of this research could drive innovations in various fields, from catalysis to advanced electronic devices.

2 Methods.

Spin-polarized DFT calculations were conducted using the Quantum ESPRESSO package [59–61]. We employed ultrasoft pseudopotentials with the GGA-PBE approach (Perdew, Burke, and Ernzerhof) for the exchange-correlation (XC) potential [62]. Additionally, we accounted for long-range dispersion-corrected van der Waals interactions utilizing the Grimme-D3 scheme [63]. Kinetic energy cutoffs were set at 30 Ry and 240 Ry for the wave function and charge density, respectively. In geometric optimization, a $\Gamma-$centered Monkhorst-Pack mesh with k-point grids of $3 \times 3 \times 1$ was applied for Brillouin zone integrations, and $9 \times 9 \times 1$ for electronic analysis [64]. We included an empty space of 20 Å perpendicular to the monolayer to prevent self-interaction due to periodic boundary conditions. The investigation of the cluster growth was carried out in a 5×5 periodicity supercell.

View Article Online
DOI: 10.1039/D4NR02713B

3 Results and Discussion.

3.1 Substrates models TM_0–NxV_2

Structural deformations in the carbon lattice tend to favor the coalition between the carbon substrate and the metallic adatoms. It is reported in the literature that the graphene lattice with two continuous carbon vacancies induces a hole that traps a metal adatom and incorporates it into the graphene lattice, generating a single-atom catalyst (SAC) model [52]. Therefore, for the initial phase of this study, we optimized the unit cell of the graphene structure to construct two carbon substrates where the cluster would interact. The optimized lattice parameter is $a_0 = 2.46$ Å, in good agreement with the experimental value [65]. Next, two graphene (5x5) models were built. The first one contains only a double vacancy (see Figure 1(a)), whereas for the second model, we employed a graphene monolayer with two carbon vacancies that contain four pyridinic nitrogen atoms substituting four carbon atoms surrounding the double vacancy (see Figure 1(b)).

These configurations are denoted as TM_n–N_4V_2 and TM_n–N_0V_2, where TM={Fe, Cu}, the index n in TM_n represents the number of transition metal (TM) atoms incorporated at the model (where n varies from 0 to 6), N_x denotes the number of incorporated pyridinic nitrogen atoms in the monolayer (in this case, four or zero), and V_2 stands for the count of vacancies within the graphene original lattice. We designate carbon atoms bonded to the TM as C_{α_1} and to N as C_{α_2}, as illustrated in Figure 1. Despite the disparity in nitrogen doping between both models, their structural resemblance is noteworthy, as both exhibit a planar structure, with C-C bond lengths of 1.42 Å and C-N bond lenghts of 1.34 Å for the nitrogenated lattice.

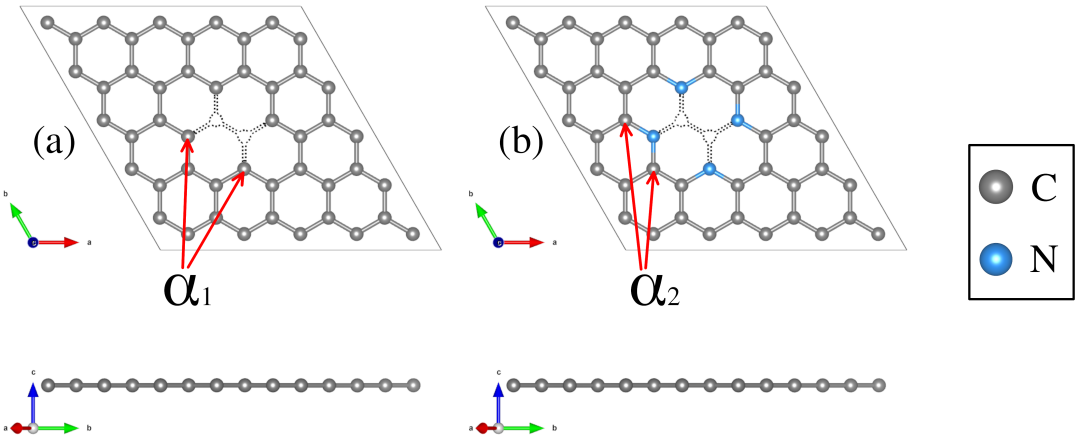

Figure 1: Structural top and side views of (a)TM–N_0V_2 and (b)TM–N_4V_2. The C, and N atoms are depicted as gray, and blue spheres.

Since both models contain different species around the vacancy where the TM atom is captured and incorporated into the lattice, we have characterized the charge distribution of the atoms around the vacancy of the clean substrates. To this end, we have employed the Bader charge (BC) formalism, which allows us to quantify the charge values associated with each atom [66, 67]. The values obtained allow us to measure changes in the charge distribution ($\Delta Q = e_{valence} - Bader$) and provide vital information on the substrate-adsorbate interaction.

Regarding the charge distribution of the substrates models, an RGB color code has been employed to differentiate between charge loss, unchanged, and gain, respectively, depending on the ΔQ values.

View Article Online
DOI: 10.1039/D4NR02713B

The charge redistribution is practically negligible when the system lacks N (see Figure 2(a)). The slight variation of ΔQ in the $TM_0{-}N_0V_2$ model is around the carbon atoms of the vacancies due to the missing bonds. In contrast, for the $TM_0{-}N_4V_2$ model (see Figure 2(b)), it is evident that the ΔQ values for the pyridinic nitrogen atoms indicate their role in inducing a redistribution of charge within the system due to the difference in electronegativity between C and N atoms. The N atoms become charge acceptors, gaining an average of -1.04e. In contrast, the C_{α_2} atoms donate charge with an average value of +0.52e, while the remaining carbon atoms in the graphene lattice remain neutral.

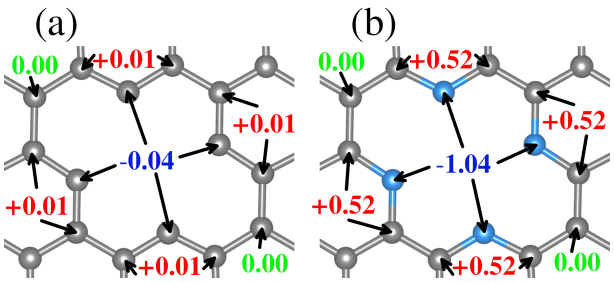

Figure 2: Bader Charges difference values per atom for the (a) $TM_0{-}N_0V_2$ system and (b) the $TM_0{-}N_4V_2$ system. An RGB color code was used to display the electronic charge loss (red), unchanged (green), or gained (blue).

3.2 Clusters Formation in $TM_n{-}NxV_2$ Models

Once the $TM_0{-}NxV_2$ substrates were structurally characterized, the systematic incorporation of Fe or Cu atoms -from one to six- in both monolayers was studied to delve into how the chemical environment on the substrates N or C_α atoms influences the TM_n adsorption states. This section thoroughly explores the one-by-one incorporation of TM_n atoms to form a cluster geometric shape. It describes their structural evolution during the growth stages, charge distribution, and magnetic and electronic properties as the TM_n cluster size increases. Furthermore, we do not combine TM species into the cluster. Fe and Cu elements were chosen due to their magnetic and non-magnetic character in their corresponding bulk phases. However, the magnetic dipole moments in both TM_n cluster cases were explored due to the small cluster size.

3.2.1 Structural characterization of Cluster Shape in $TM_n{-}NxV_2$.

Two substrate models have been selected, four systems were considered for systematically incorporating Fe and Cu atoms -each atom on $TM_n{-}N_0V_2$ and $TM_n{-}N_4V_2$-. For the next part of the study, we refer to each adatom incorporation with the notation $TM\#1$, where n ranges between one and six.

The first incorporation of the TM atom ($TM\#1$) into both substrates ($TM_1{-}NxV_2$) was favored at the C vacancies. These are the most favorable structural models for the initial TM adsorption, as depicted in Figure 3 (a-1), (b-1), (c-1), and (d-1) for $Cu_1{-}N_4V_2$, $Cu_1{-}N_0V_2$, $Fe_1{-}N_4V_2$, and $Fe_1{-}N_0V_2$, respectively, leading to a planar model with the formation of two pentagonal rings and two hexagonal rings (additional views of the adsorption states are shown in Figure S1-1).

For the next TM incorporation, the $TM_2{-}NxV_2$ minimum energy models are illustrated in Figure 3(a-2,b-2,c-2,d-2). In the case of $Cu_2{-}N_4V_2$, the second Cu atom ($Cu\#2$) achieves a two-fold coordination with bonds to the first Cu atom ($Cu\#1$) and to a neighboring N atom in a bridge-type position, as shown in Figure 3(a-2). Meanwhile, in the $Cu_2{-}N_0V_2$ structure, $Cu\#2$ is located over

View Article Online
DOI: 10.1039/D4NR02713B

a hexagonal ring, reaching a three-fold coordination with $Cu\#1$ and two C_{α_1} atoms, as depicted in Figure 3(b-2). In contrast, the $Fe_2{-}N_4V_2$ model's second Fe atom ($Fe\#2$) does not form bonds with lattice and remains in a top position above $Fe\#1$, as shown in Figure 3(c-2). Finally, in the $Fe_2{-}N_0V_2$ structure, a subtle deformation in the carbon system emerges; $Fe\#2$ binds to two C_{α_1} atoms, forming a hexagonal ring with the lattice and laying over the substrate. As a result, this model is no longer planar. $Fe\#2$ bonds to $Fe\#1$, driving it down the lattice and creating a symmetrical model. In this configuration, $Fe\#1$ is now bonded to only two C_{α_1} atoms, instead of four C_{α_1} as in the $TM_1{-}N_0V_2$, as shown in Figure 3(d-2). The $Fe_2{-}N_0V_2$ model does not present pentagonal rings since the Fe-Fe bond turns them into hexagonal non-planar rings (see Figure S1-1). Accordingly, there are already evident geometrical differences between the four $TM_2{-}NxV_2$ models. The differences are influenced by a combination of factors. For example, in the case of the copper models ($Cu_2{-}N_4V_2$ and $Cu_2{-}N_0V_2$), the second copper atom can form different types of bonds depending on its local environment. This is because copper can have different oxidation states and coordination geometries, which influence how it bonds with neighboring nitrogen and carbon atoms. In contrast, in the iron models ($Fe_2{-}N_4V_2$ and $Fe_2{-}N_0V_2$), the second iron atom tends to maintain a higher position above the carbon substrate. This may be due to the unique magnetic and electronic properties of iron, which can influence its interaction with the carbon network and affect its ability to form bonds with other atoms. Additionally, differences in the structure of the models may be related to the availability of binding sites and the stability of the formed bonds. For instance, in the case of the $Fe_2{-}N_0V_2$ model, subtle deformation in the carbon network may be influenced by the interaction between iron atoms and nearby carbon atoms, resulting in a more complex and non-planar structure.

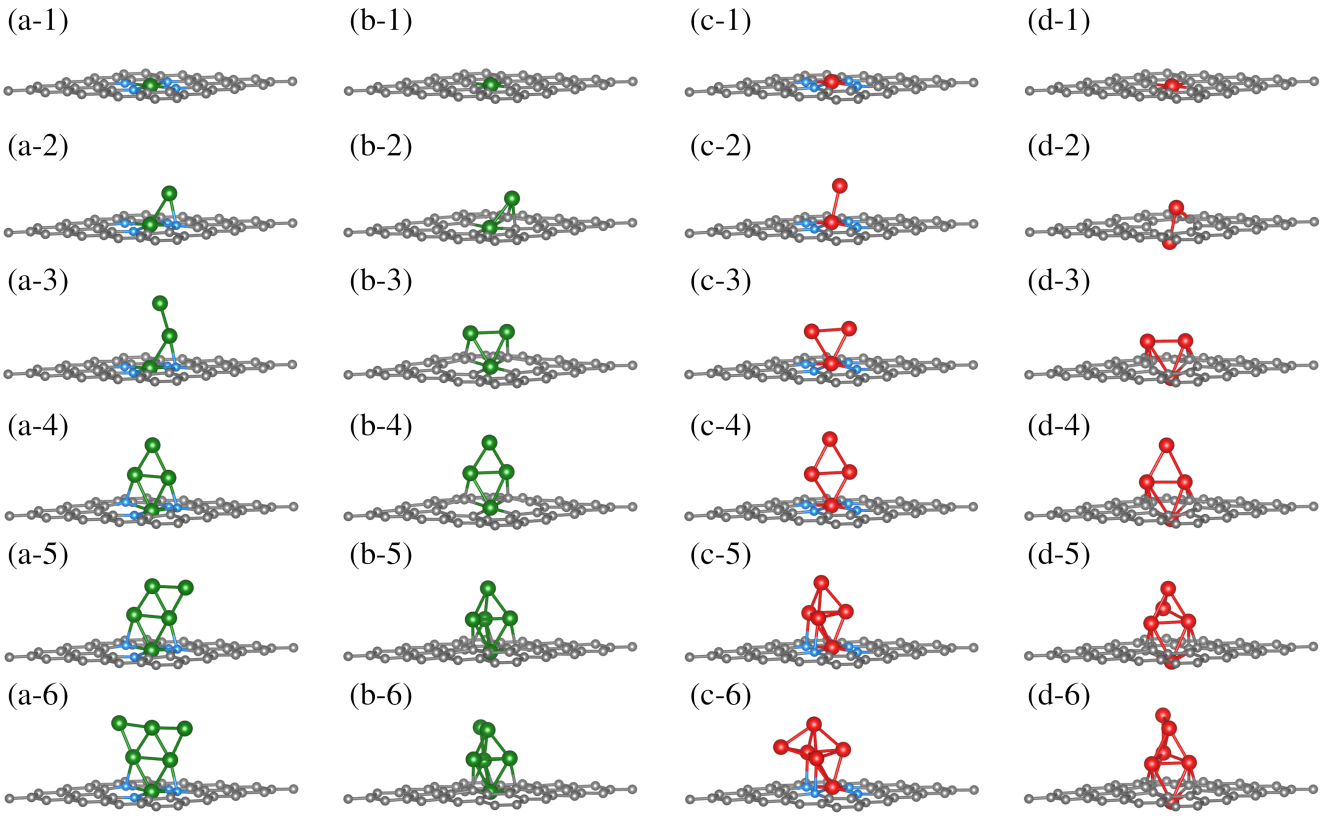

Figure 3: Growth Mechanism of Clusters in $TM_n{-}NxV_2$ Systems. The growth within the same system is observed horizontally, and the same growth stage is presented vertically for different systems. The C, N, Cu, and Fe atoms are depicted as dark, blue, green, and red spheres. For additional views of these configurations, refer to Figure SI1

View Article Online
DOI: 10.1039/D4NR02713B

The subsequent incorporation of TM is related to the TM_3–NxV_2 models. An open structure constitutes the most stable model for $Cu\#3$ on TM_3–N_4V_2. $Cu\#3$ only bonds with $Cu\#2$, whereas the rest of the model remains unchanged, extending the Cu-cluster shape upward, as depicted in Figure 3(a-3). On the other hand, $Cu\#3$ in Cu_3–N_0V_2 forms three chemical bonds, binding with the pair of Cu atoms ($Cu\#1$ and $Cu\#2$), and a C_{α_1}. Moreover, the $Cu\#2$ atom also reaches three-fold coordination. However, instead of being bound with two C_{α_1} as in Cu_2–N_0V_2, it bounds to one C_{α_1} and the other two Cu atoms, forming a triangular shape as shown in Figure 3(b-3). The C_{α_1} atoms bonded to Cu atoms are in the same pentagonal ring. The Fe_3–NxV_2 holds a triangular shape for the Fe atoms on both substrates. However, only $Fe\#1$ is bonded to the four N atoms along the monolayer plane, while neither $Fe\#2$ nor $Fe\#3$ bonds to any substrate atom. In this configuration, the Fe_3 triangle cluster lies perpendicular to the substrate plane, positioning $Fe\#2$ and $Fe\#3$ over opposite hexagonal rings (Figure 3(c-3)). On the other hand, in Fe_3–N_0V_2, since $Fe\#1$ has crossed the substrate lattice, $Fe\#2$ and $Fe\#3$ bond to two C_{α_1} each. Fe_3–N_0V_2 presents a more significant number of chemical bonds, as shown in Figure 3(d-3). Furthermore, in Cu_3–N_0V_2, Fe_3–N_4V_2, and Fe_3–N_0V_2, the TM cluster shape induces a similar chemical environment for $TM\#2$ and $TM\#3$; that is to say, these are atoms with equivalent bond symmetries.

The fourth TM incorporation generates the TM_4–NxV_2 models shown in Figure (a-4,b-4,c-4,d-4). Note that in the Cu_4–NxV_2 model, three Cu atoms are chemically bonded to the substrate. On the nitrogenated substrate, $Cu\#1$ bonds to all N atoms; $Cu\#2$ and $Cu\#4$ bond to an opposite N atom in Cu_4–N_4V_2 (Figure 3(a-4). Meanwhile, in Cu_4–N_0V_2, $Cu\#4$ is the Cu atom that does not bind to the substrate (Figure 3(b-4), and as described in the Cu_3–N_0V_2 model, $Cu\#2$ and $Cu\#3$ bond to adjacent C_{α_1} in a pentagonal ring. For Fe_4–N_4V_2, $Fe\#1$ is still the only Fe atom of the Fe_4 cluster that is chemically bonded to the substrate; the other three Fe atoms bond only to Fe atoms, adopting a perpendicular planar configuration (Figure 3(c-4). On the other hand, in Fe_4–N_0V_2, $Fe\#4$ is the only Fe atom that doesn't bond to the substrate, and the rest of the Fe atoms remain unchanged compared with the Fe_3–N_0V_2 model (Figure 3(c-4). The TM_4–NxV_2 model form rhomboidal cluster shapes across the substrates except for Cu_4–N_0V_2, where the rhombohedral cluster shape is planar and perpendicular to the monolayer (see Figure S1(a-d)4). Additionally, the TM_4 cluster induces an identical adsorption position for $TM\#2$ and $TM\#3$, generating a triangular configuration with $TM\#1$.

The subsequent incorporation generates the TM_5–NxV_2 models. For $Cu\#5$ on the nitrogenated substrate (TM_5–N_4V_2), a semi-triangular cluster shape is generated where $Cu\#5$ is two-fold coordinated with the $Cu\#4$ atom and a Cu atom that interacts with an N atom from the substrate (Figure 3(a-5). For the TM_5–N_0V_2 substrate, the $Cu\#5$ atom reaches a three-fold coordination with three Cu atoms, completing a rhombohedral shape (Figure 3(b-5). For the addition of Fe atoms, the $Fe\#5$ atom also reaches a similar configuration to the previously described $Cu\#5$ over the TM_5–N_4V_2 substrate, while on TM_5–N_0V_2 the same cluster shapes emerge. In this configurations, a pair of Fe atoms supporting the top $Fe\#5$ atom of the rhombohedral cluster establishes an interaction with the surface.

Finally, we present the TM_6–NxV_2 models. In the Cu_6–N_4V_2 model, the Cu_6 cluster mantains its planar arrangement, forming a planar triangular cluster. In the Cu_6–N_0V_2 model, $Cu\#6$ bonds with two Cu atoms ($Cu\#4$ and $Cu\#5$) in a bridge position, as shown in Figure 3(b-6). For the Fe_6–N_4V_2 model, $Fe\#6$ bonds to three Fe atoms without interacting with the surface atoms, as shown in Figure 3(c-6). Meanwhile, in the Fe_6–N_0V_2 model, $Fe\#6$ similarly binds to the Fe-cluster as $Cu\#6$ does in forming the Cu_6 cluster. In addition, the optimized structures of free-standing Cu/Fe clusters, independent of the substrate, are provided in the Supplementary Information (S2).

View Article Online
DOI: 10.1039/D4NR02713B

3.2.2 TM_n–NxV_2 charge distribution.

We analyzed the electronic charge distribution after describing the structural models of TM_n–NxV_2. A Bader difference charge calculation ΔQ, defined in section 3.1, was employed to comprehensively understand charge distribution throughout the cluster size increment in the TM_n–NxV_2 models. The calculated ΔQ per TM atom for the different cluster sizes are depicted in Figure 4. The RGB color codes employed are red, green, and blue for charge loss, unchanged, and gain.

All TM display charge loss upon joining the substrate for the first TM incorporation. Notably, a discernible trend exists where $TM\#1$ tends to lose more electronic charge in a nitrogen-rich environment. This trend is primarily attributed to nitrogen's role as a charge acceptor, as shown in the first row of Figure 4. On the nitrogenated substrates, Cu loses +0.93e while Fe loses +1.18e; on the TM_1–N_0V_2 substrate the values are +0.65e and +0.98e for Cu, and Fe.

In contrast to TM_1–NxV_2, in the TM_2–NxV_2 models, $TM\#1$ reduces its charge donation value to the substrate, and in all cases, $TM\#2$ also shows an electronic donor charge character. As described in the structural section, since the $TM\#2$ chemical environment is distinct in each TM_2–NxV_2 model, $TM\#2$ yields different amounts of charge. In Cu_2–N_4V_2, $Cu\#2$ (bonded to $Cu\#1$ and a N atom) gives +0.14e, in addition to the +0.86e provided by $Cu\#1$, resulting in the entire Cu_2 cluster giving +1.00e to the substrate (see Figure 4(a-2)). Meanwhile, in Cu_2–N_0V_2, $Cu\#2$ (bonded to $Cu\#1$ and two C_{α_1}) yields +0.46e, and $Cu\#1$ yields +0.61e. Hence, the Cu_2 cluster gives a total of +1.07e to the substrate (see Figure 4(b-2)). In Fe_2–N_4V_2, $Fe\#1$ and $Fe\#2$ provide +0.99e and +0.26e, respectively, as shown in Figure 4(c-2); therefore, the Fe_2 cluster yields +1.25e to the substrate. In Fe_2–N_0V_2, the Fe_2 cluster yields +1.61e; since both Fe atoms have a similar chemical environment, the calculated ΔQ for each Fe atom is almost identical (see Figure 4(d-2)). All the calculated ΔQ per TM atom and the clusters' ΔQ are shown in Figure 4.

The clusters composed by a third TM atom (TM_3–NxV_2) present a donor charge character except for the Cu_3–N_4V_2 model where the third adatom presents an electron gain value of -0.16e, and the previously had values +0.19e and +0.89e. Note that the coordination of this atom is single-bonded with the previous Cu atom. In contrast, for the other TM_3–NxV_2 models, the incorporated atoms are two-fold coordinated with the previous TM atoms, and interaction with the substrate for the second and third TM is also evident for the substrates without N. The total cluster charge values are +0.92, +1.07, +1.50, and +1.87 for Cu_3–N_4V_2, Cu_3–N_0V_2, Fe_3–N_4V_2, and Fe_3–N_0V_2 respectively (see Figure 4(a-d3)).

With the fourth TM incorporation and the formation of a planar cluster for the studied models, the $TM\#4$ atom does not interact with the substrate. It is only two-fold coordinated with the contiguous TM atoms, presenting a charge acceptor character. For Cu_4–N_4V_2 (Figure 4(a-4)), the charge values are -0.16e, +0.31e, +0.31e, and +0.79e, providing a total cluster charge of +1.25e. In Cu_4–N_0V_2, the same trend appears with charge values of -0.08e, +0.29e, +0.29e, and +0.60e for a total of +1.1e for the complete cluster. The same trend is observed for the Fe cluster, where the Fe atoms had charge values of -0.09e and -0.10e for Fe_4–N_4V_2 and Fe_4–N_0V_2. Accordingly, the cluster charge values are +1.25, +1.09, +1.47, and +1.77. In this case, although the $TM\#4$ atom accepts a minimal charge, its role as an acceptor suggests a unique dynamic in the system. This is due to its position and interactions with neighboring atoms, where factors like low electron density and electrostatic forces may have an influence. Such behavior underscores the complexity of these systems, where slight variations have significant impacts on their behavior and properties.

View Article Online
DOI: 10.1039/D4NR02713B

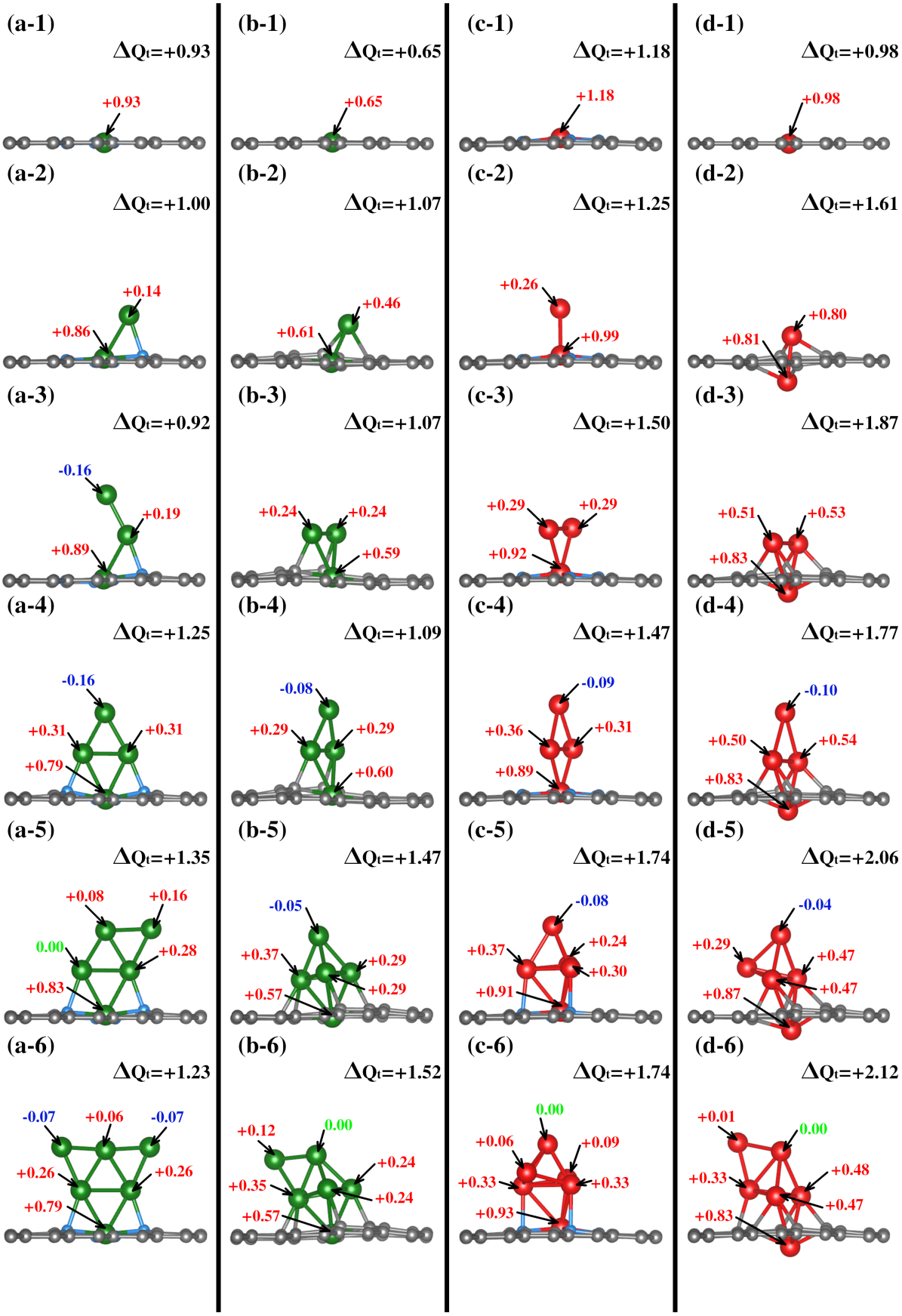

Figure 4: Bader charges are monitored throughout the growth mechanism of each system, with each row corresponding to the same state observed in different systems and each column depicting the growth pathway for a specific system.

View Article Online
DOI: 10.1039/D4NR02713B

The subsequent incorporation of atoms generates the $TM\#5$ models, Except for the semi triangular Cu_5–N_4V_2 cluster, where the added Cu atom acts as a charge donor with a value of +0.16e, the rhombohedral clusters with the TM at the tip present a ΔQ gain of -0.05e, -0.08e and -0.04e for Cu_5–N_0V_2, Fe_5–N_4V_2, and Fe_5–N_0V_2, respectively. The cluster charge values are +1.35, +1.47, +1.74, and +2.06.

Finally, for the clusters formed by six atoms, it is observed that the triangular planar cluster has a charge acceptor character at the edges -two-fold coordinated Cu atoms- with values of -0.07e. The remaining systems, which form rhombohedral clusters, show a TM with unchanged charge $\Delta Q = 0$. The total charge migration values are +1.23, +1.52, +1.74, and +2.21 for Cu_6–N_4V_2, Cu_6–N_0V_2, Fe_6–N_4V_2, and Fe_6–N_0V_2, respectively.

Overall, throughout the growth process, the TM_n cluster donates electronic charge to the substrates. Additionally, atoms within each TM_n cluster with equivalent chemical environments exhibit the same ΔQ value.

3.2.3 TM_n–NxV_2 magnetic properties.

For a better understanding of the magnetic properties throughout the cluster growth, the magnetic moments of each atom in the TM_n–NxV_2 systems were characterized, as shown in Figure 5, . Additionally, Table 1 presents the contributions to the total magnetization from both the cluster and the substrate.

System	Cu–N_4V_2 (μ_B)			Cu–N_0V_2 (μ_B)			Fe–N_4V_2 (μ_B)			Fe–N_0V_2 (μ_B)		
	M_T	M_{Cl}	M_{subs}	M_T	M_{Cl}	M_{subs}	M_T	M_{Cl}	M_{subs}	M_T	M_{Cl}	M_{subs}
TM_1	1.00	0.46	0.54	0.00	0.00	0.00	2.00	1.98	0.02	2.07	1.30	0.77
TM_2	1.58	0.98	0.60	0.00	0.00	0.00	4.02	4.00	0.02	4.03	4.36	-0.33
TM_3	0.86	0.34	0.52	0.00	0.00	0.00	7.94	7.97	-0.03	7.99	7.78	0.21
TM_4	0.73	0.28	0.45	0.00	0.00	0.00	6.07	6.22	0.14	10.03	10.16	-0.13
TM_5	-1.00	-0.48	-0.52	0.00	0.00	0.00	3.98	4.01	-0.03	14.04	13.71	0.34
TM_6	-0.77	-0.38	-0.38	0.00	0.00	0.00	16.01	16.19	-0.18	12.08	12.09	-0.01

Table 1: Contribution to magnetization in each system is delineated. M_T denotes the total magnetization of the system, M_{Cl} represents the magnetization of the cluster, and M_{subs} stands for the magnetization associated with the substrate.

Between the Cu–N_4V_2 and Cu–N_0V_2 systems, the main distinction lies in the total magnetization of the structure. In Cu–N_4V_2, there is consistently intrinsic magnetization in the system. In contrast, the Cu–N_0V_2 structures exhibit negligible magnetization throughout the cluster growth, as depicted in Fig 5 columns a and b. This suggests that Cu in a nitrogen-free environment does not induce polarization in the substrate, unlike in an environment with nitrogen (refer to Table 1). Additionally, it is noteworthy that as the cluster grows in Cu–N_4V_2, the Cu atoms in the monolayer exhibits significant magnetic characteristics. This point is attributed to forming bonds with nitrogen, inducing a magnetic moment in Cu. This can be observed in Figures 5 (a-3), (a-4), (a-5), and (a-6), where the copper in the monolayer displays the highest magnetic moments of +0.43 μ_B, +0.27 μ_B, +0.36 μ_B, and -0.31 μ_B, respectively.

View Article Online
DOI: 10.1039/D4NR02713B

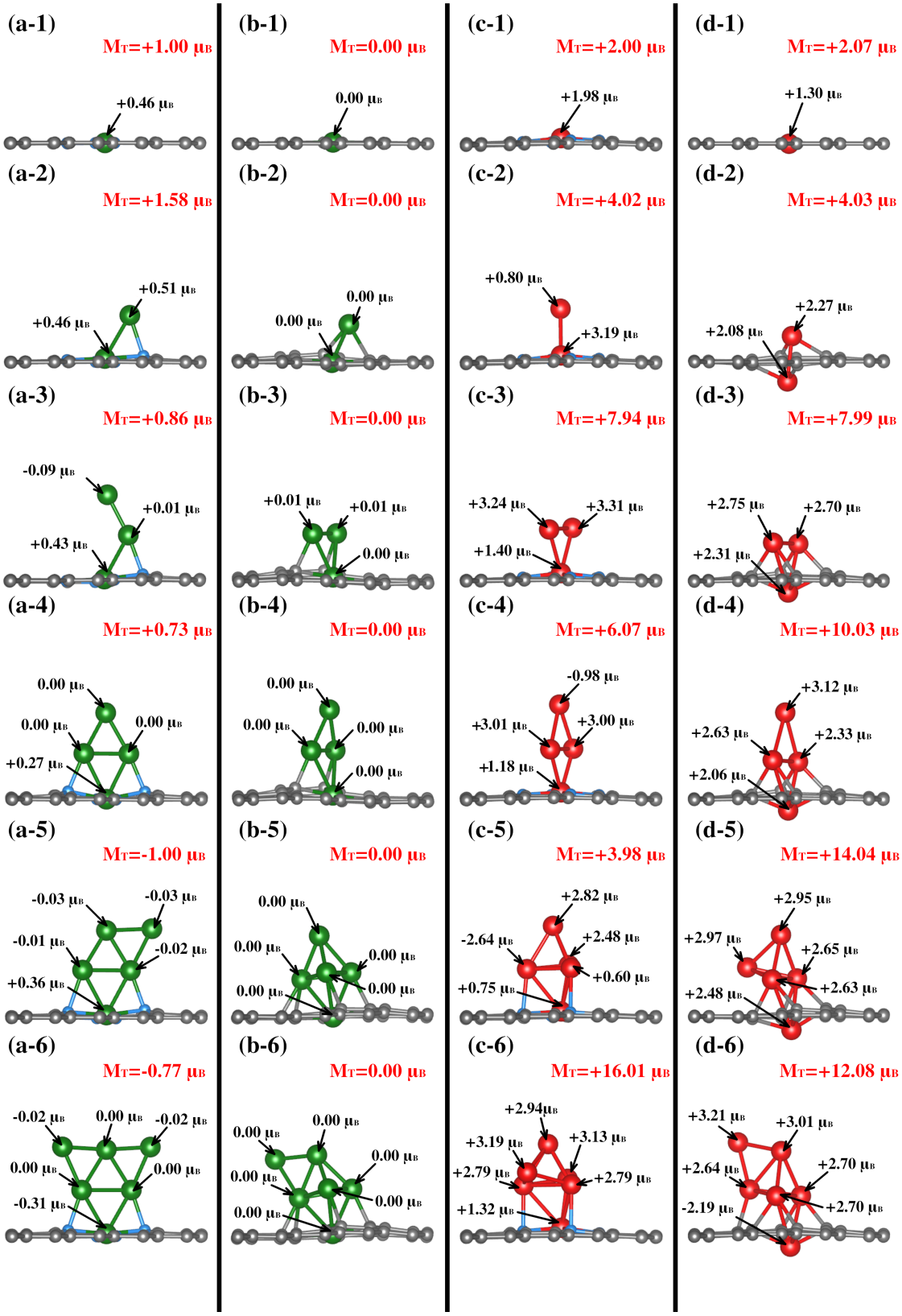

Figure 5: Magnetic moments of each metal site for the TM_n-NxV_2 systems are presented. The total magnetization of each system is depicted in red. Panels (a) through (d) correspond to $Cu-N_4V_2$, $Cu-N_0V_2$, $Fe-N_4V_2$, and $Fe-N_0V_2$, respectively.

View Article Online
DOI: 10.1039/D4NR02713B

In the case of the Fe−NxV_2 structures, Table 1 reveals that in structures with N, the primary contribution to the total magnetization comes from the cluster, with minimal contribution from the substrate. This is attributed to Fe being inherently magnetic, and the presence of N does not significantly affect its polarization throughout the cluster growth. On the other hand, in the Fe−N_0V_2 structures, Table 1 suggests a more substantial contribution from the substrate, as observed in Fig. 5 (d-1). In this case, the substrate contributes +0.77 μ_B, adding to the +1.30 μ_B from Fe, resulting in a total magnetization of +2.07 μ_B. It is noteworthy that, unlike iron, the presence of nitrogen is crucial for inducing polarization in the Cu species. This observation can be elucidated by considering the electronic and chemical interactions within the Cu-N systems. Cu is a transition metal with partially filled d-orbitals, making it inherently susceptible to magnetic moments. However, in the absence of specific external influences, the magnetic behavior of copper might remain relatively subdued. The introduction of nitrogen into the system creates a dynamic environment where the Cu atoms interact with the nitrogen atoms, forming Cu-N bonds. These bonds can introduce unpaired electrons and alter the electronic configuration of the Cu atoms. The interaction with nitrogen induces a magnetic polarization in the Cu species, enhancing its magnetic characteristics. In contrast, Fe is already a well-known magnetic species due to its intrinsic magnetic moments arising from its electron configuration. Therefore, in the Fe-N systems, nitrogen impact on iron magnetic behavior may be comparatively less pronounced. Fe's inherent magnetism is less influenced by nitrogen, resulting in a more consistent magnetic behavior throughout the cluster growth.

3.2.4 TM_n–NxV_2 electronic properties.

To enhance our comprehension of the electronic structure within each system, we have generated density of states plots of the entire growth mechanism, as illustrated in Figure 6. In the case of the Cu−N_4V_2 system, as depicted in Figure 6(a-1), it can be seen that in the vicinity of the Fermi level, the contributions of nitrogen coincide with those of copper, indicating the interaction between Cu and N. In the case of $2Cu_2$−N_4V_2, the Cu contributions intensify, exhibiting well-defined peaks around -2 eV (Figure 6(a-2)). As the cluster size increases, the Cu contributions continue to grow, providing evidence of an increased Cu presence in the system and, consequently, a more pronounced interaction between the monolayer and the cluster.

In the case of Cu−N_0V_2, where nitrogen is absent, copper (Cu) exhibits contributions at the same energy level and slightly to the right (Figure 6(b-1)). This observation indicates the stability that copper gains when it incorporates embedded nitrogen within the monolayer. As the cluster grows, the Cu contributions increase in intensity, consistently remaining around -2 eV.

In the context of the Fe−N_4V_2 system, which is presented in Figure 6(c-1), it is worth highlighting the position of the contributions in relation to the formation of N-Fe bonds. These contributions are observed at approximately 2 eV, which is slightly to the right compared to their counterparts in the case of copper (Cu). This difference in positioning suggests distinct energy requirements and behaviors for bond formation between nitrogen and iron as opposed to nitrogen and copper. Furthermore, as the cluster size increases, we notice an intriguing phenomenon. The intensity of the iron (Fe) contributions intensifies, indicating an enhanced presence of iron atoms in the system. However, this observation is particularly intriguing because these contributions do not maintain a uniform energy level. Instead, they are distributed at various energy levels, indicating a diverse range of bonding configurations or states within the growing cluster.

View Article Online
DOI: 10.1039/D4NR02713B

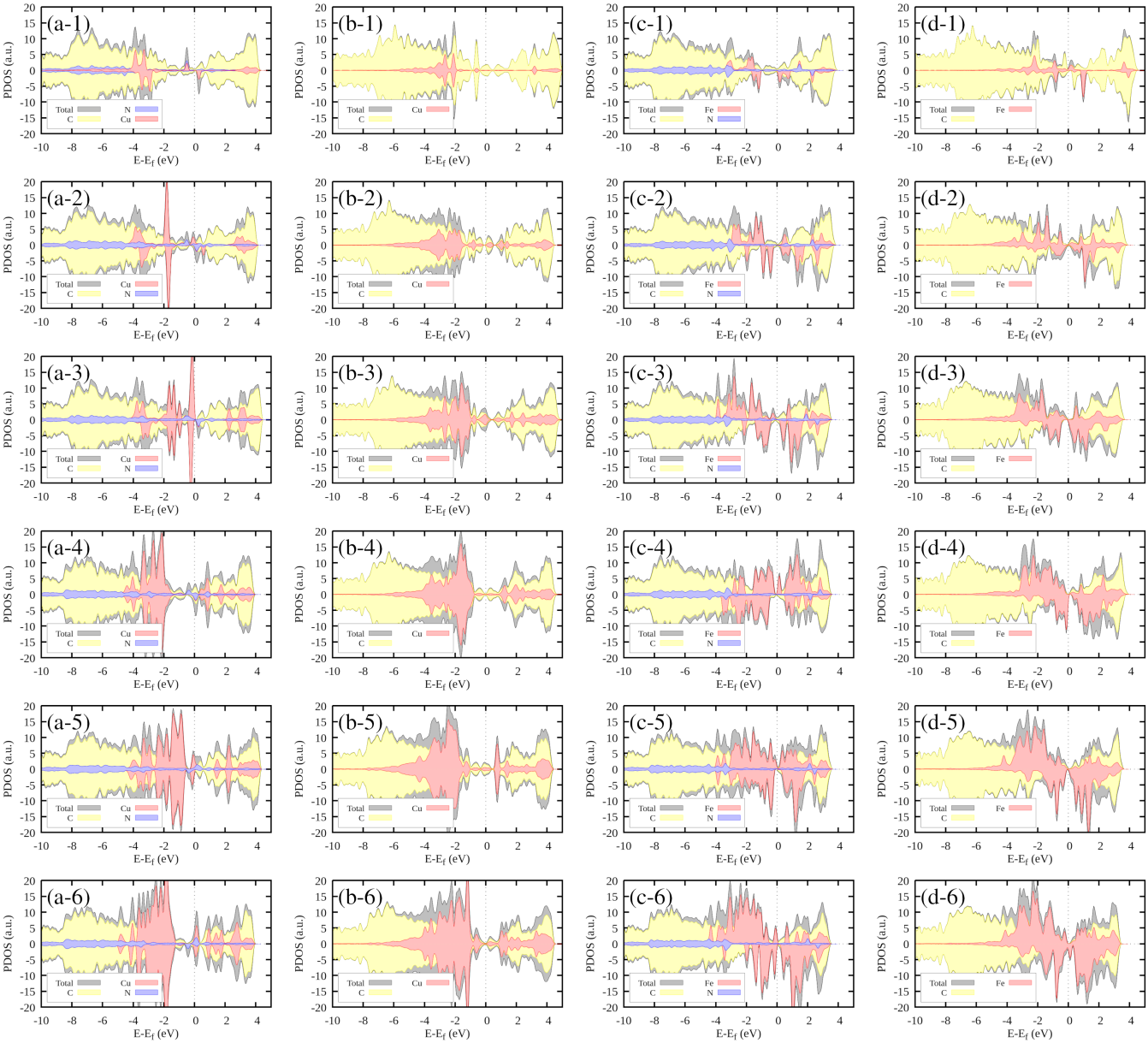

Figure 6: Projected Density of States (PDOS) is presented for (a) Cu−N_4V_2, (b) Cu−N_0V_2, (d) Fe−N_4V_2, and (e) Fe−N_0V_2 systems. The total system contribution is shown in black; the yellow segment represents the contribution from carbon (C) atoms, and the blue component shows the contribution from nitrogen (N) atoms. The red segment corresponds to the transition metal (TM), which can be either copper (Cu) or iron (Fe).

Finally, in the case of the Fe−N_0V_2 system (Figure 6(d-1)), we can observe a similar trend to the previous scenario. The behavior of the Fe contributions manifests at varying energy levels, displaying significant asymmetry between the spin-up and spin-down states. This asymmetry in the energy distribution further underscores the intricate electronic properties of the growing cluster, shedding light on the complexity of the Fe-C interactions in the absence of nitrogen.

In Figure S3-1 of the supplementary information, the DOS contribution from the most exposed transition metal in the system is highlighted in green. Notably, the contributions closest to the Fermi level, indicative of electronic states readily available for interaction, predominantly originated by the most exposed TMs. This observation hints at the unique electronic influence exerted by the most

View Article Online
DOI: 10.1039/D4NR02713B

exposed TM within the cluster. Its distinct positioning or bonding characteristics likely facilitate localized electronic interactions, resulting in the emergence of prominent electronic states near the Fermi level. These states, in turn, play a pivotal role in shaping the electronic properties of the entire system, particularly in the vicinity of the Fermi energy.

3.2.5 TM_n–NxV_2 growth and aggregation analysis.

To gain a better understanding of cluster size with N-doped and non N-doped substrates, we utilized the formalism of growth and aggregation energies, as described by equations 1 and 2, respectively. In this way, we focus on identifying the chemical environment that may promote TM clusters' dispersion, growth, or aggregation. This formalism is very important because its capability to quantitatively assess the energetic aspects of cluster formation and evolution, facilitating a rigorous analysis of the stability and kinetics of the cluster growth process [68].

$$E_{grow}\left[\frac{n}{n-1}\right] = [E(TM_n/slab) + E(slab)] - [E(TM_{n-1}/slab) + E(TM_1/slab)] \quad (1)$$

$$E_{agg}\frac{(n)}{n} = \frac{[E(TM_n/slab) + (n-1)E(slab) - nE(TM_1/slab)]}{n} \quad (2)$$

The E_{grow} and E_{agg} values denote the growth and aggregation energies, respectively. E_{grow} compares the TM_n cluster against $TM_n{}^{-}{}_1$ with a dispersed TM to analyze the one-atom growth mechanism. Meanwhile, E_{agg} compares the TM_n clusters with the n-TM dispersed. As the equations are expressed, negative E_{grow} or E_{agg} values indicate a thermodynamically more favorable configuration. This means that growth or aggregations are viable, respectively. E($TM_n/slab$) is the TM_n–NxV_2 total energy, and E(slab) is the substrate energy.

We will first discuss the E_{grow} results. Regarding the growth energies, as depicted in Figure 7(a), it is evident that in the initial step, all the TM_2–NxV_2 systems exhibit positive growth energies. Physically, considering equation 1, this means a greater likelihood of adatoms arriving at vacancies rather than cluster growth. In this case, the positive energy values indicate that the influx of adatoms favors the saturation of vacancies before cluster growth, a trend observed across all systems. If controllable incorporation of TM into carbon substrates could be achieved through high vacuum synthesis methods like magnetron sputtering, inert gas condensation, and soft-landing techniques (as clarified in the introduction section), then highly dispersed SACs could be obtained, provided that two carbon vacancies are present at the substrate. It is noteworthy that the Fe_2–N_0V_2 system has the lowest E_{grow} value of 0.21 eV. Meanwhile, the N-doped substrates present the highest E_{grow} values.

View Article Online
DOI: 10.1039/D4NR02713B

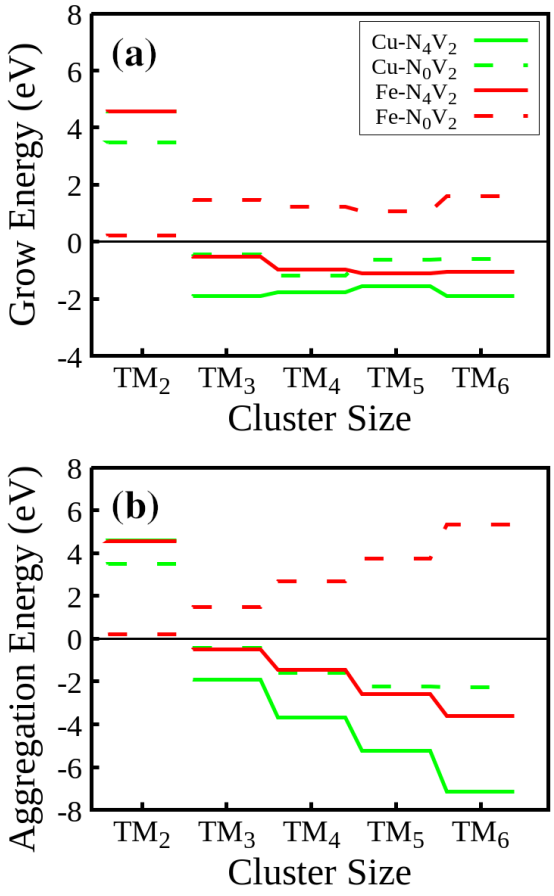

Figure 7: (a) Growth energies and (b) Aggregation energies for TM-NxV2 structures during cluster formation.

The cluster growth will only occur once the vacancies are filled with the first TM. From now on, we will consider TM_1–NxV_2 as E(slab) in equation 1. Once the vacancies are saturated and more TM are incorporated into the system, one-atom cluster growth becomes feasible for Cu regardless of the presence of nitrogen, as evidenced by the negative E_{grow} value. Meanwhile, Fe cluster growth is only viable in the nitrogenate substrate, since the Fe–N_0V_2 E_{grow} are positive.

In terms of the aggregation energies, as described by equation 2 and illustrated in Figure 7(b), we can observe that the E_{agg} values for clusters made of two atoms are positive. This observation confirms that it is imperative to first saturate the vacancies with a TM before cluster growth or aggregation in any system. Once this step is accomplished, the TM cluster aggregation becomes feasible for the Cu clusters on both substrates and the Fe cluster on the N-doped monolayer due to the E_{agg} negative value.

These findings on aggregation and growth energies suggest that once all vacancies are saturated by a TM, a nitrogen-rich environment promotes the cluster growth mechanism, enabling systems to achieve increased stability as the growth process go on. This observation aligns with findings in published studies that have highlighted the role of nitrogen in modulating the properties and chemical reactivity of materials [51, 55]. Specifically, these studies have emphasized the influence of nitrogen on the selectivity of specific reactions, such as the oxygen reduction reaction (ORR), where the presence of nitrogen in nitrogen-doped graphitic carbon materials has been shown to affect the preferred reaction pathway [51]. This consistency among findings underscores the significance of nitrogen in materials engineering for specific applications in fields like energy and the environment.

View Article Online
DOI: 10.1039/D4NR02713B

4 Conclusions.

In this study, we investigated the growth mechanism of Cu and Fe clusters on a graphene monolayer, particularly examining scenarios with and without nitrogen doping (TM_n–NxV_2). Our analysis reveals intriguing growth patterns, especially within Cu-based systems. The presence of pyridine nitrogen induces a more structured and orderly growth of Cu clusters, forming a stable plane perpendicular to the monolayer. In contrast, in nitrogen-deficient environments, Cu clusters exhibit less organized, more clumped formations.

Pyridine nitrogen also plays a crucial role in improving the structural stability of Fe clusters, reducing the deformations often observed in its absence. Additionally, nitrogen facilitates magnetization in Cu_n–N_4V_2 systems and focuses the magnetic properties in Fe clusters.

Using the formalism of aggregation and growth energies, we explored system stability, highlighting nitrogen as a key factor in enhancing stability, particularly favoring Cu cluster growth. Notably, as cluster size increases, this stabilizing effect diminishes, suggesting a transition towards bulk-like behavior similar to Fe. These findings provide a deeper understanding on how pyridine nitrogen affects growth dynamics and catalytic properties, offering valuable insights for designing electrocatalysts. Understanding the minimum cluster size before transitioning to metallic behavior, similar to bulk iron, is crucial for influencing material reactivity and catalytic properties. These insights are essential for tailoring materials for improved electrocatalytic performance, with applications ranging from renewable energy generation to environmental cleanup.

View Article Online
DOI: 10.1039/D4NR02713B

Acknowledgments.

The authors thank the financial support provided through DGAPA-UNAM with projects IN102725, IN111223, and IG101124. Calculations were performed in the DGTIC-UNAM Supercomputing Center projects LANCAD-UNAM-DGTIC-051, LANCAD-UNAM-DGTIC-382, and LANCAD-UNAM-DGTIC-368. J.I.P.O thanks DGAPA-UNAM for a postdoctoral position.

References

(1) Tang, Y.; Yang, Z.; Dai, X. Trapping of metal atoms in the defects on graphene. *The Journal of Chemical Physics* **2011**, *135*, 224704.

(2) Chai, B.; Peng, T.; Mao, J.; Li, K.; Zan, L. Graphitic carbon nitride (g-C3N4)–Pt-TiO2 nanocomposite as an efficient photocatalyst for hydrogen production under visible light irradiation. *Phys. Chem. Chem. Phys.* **2012**, *14*, 16745–16752.

(3) Zhang, Y.-H. et al. Tuning the magnetic and transport property of graphene with Ti atom and cluster. *Computational Materials Science* **2012**, *56*, 95–99.

(4) Üzengi Aktürk, O.; Tomak, M. Au_nPt_n clusters adsorbed on graphene studied by first-principles calculations. *Phys. Rev. B* **2009**, *80*, 085417.

(5) Rêgo, C. R. C.; Tereshchuk, P.; Oliveira, L. N.; Da Silva, J. L. F. Graphene-supported small transition-metal clusters: A density functional theory investigation within van der Waals corrections. *Phys. Rev. B* **2017**, *95*, 235422.

(6) Yoo, E. et al. Enhanced Electrocatalytic Activity of Pt Subnanoclusters on Graphene Nanosheet Surface. *Nano Letters* **2009**, *9*, 2255–2259.

(7) Yan, H. et al. Single-Atom Pd1/Graphene Catalyst Achieved by Atomic Layer Deposition: Remarkable Performance in Selective Hydrogenation of 1, 3-1Butadiene. *Journal of the American Chemical Society* **2015**, *137*, 10484–10487.

(8) Hussain, R. et al. Density functional theory study of palladium cluster adsorption on a graphene support. *RSC Adv.* **2020**, *10*, 20595–20607.

(9) Manadé, M.; Viñes, F.; Illas, F. Transition metal adatoms on graphene: A systematic density functional study. *Carbon* **2015**, *95*, 525–534.

(10) Lima, M. P.; da Silva, A. J. R.; Fazzio, A. Adatoms in graphene as a source of current polarization: Role of the local magnetic moment. *Phys. Rev. B* **2011**, *84*, 245411.

(11) Acosta, C. M.; Lima, M. P.; Miwa, R. H.; da Silva, A. J. R.; Fazzio, A. Topological phases in triangular lattices of Ru adsorbed on graphene: Ab initio calculations. *Phys. Rev. B* **2014**, *89*, 155438.

(12) Dai, X.-Q.; Tang, Y.-N.; Zhao, J.-H.; Dai, Y.-W. Absorption of Pt clusters and the induced magnetic properties of graphene. *Journal of Physics: Condensed Matter* **2010**, *22*, 316005.

(13) Okazaki-Maeda, K.; Morikawa, Y.; Tanaka, S.; Kohyama, M. Structures of Pt clusters on graphene by first-principles calculations. *Surface Science* **2010**, *604*, 144–154.

(14) Sahoo, S.; Gruner, M. E.; Khanna, S. N.; Entel, P. First-principles studies on graphene-supported transition metal clusters. *The Journal of Chemical Physics* **2014**, *141*, DOI: 10.1063/1.4893328.

(15) Johll, H.; Wu, J.; Ong, S. W.; Kang, H. C.; Tok, E. S. Graphene-adsorbed Fe, Co, and Ni trimers and tetramers: Structure, stability, and magnetic moment. *Physical Review B* **2011**, *83*, DOI: 10.1103/physrevb.83.205408.

(16) Longo, R. C.; Carrete, J.; Ferrer, J.; Gallego, L. J. Structural, magnetic, and electronic properties of Ni_n and Fe_n nanostructures ($n = 1 - -4$) adsorbed on zigzag graphene nanoribbons. *Phys. Rev. B* **2010**, *81*, 115418.

(17) Diéguez, O.; Alemany, M. M. G.; Rey, C.; Ordejón, P.; Gallego, L. J. Density-functional calculations of the structures, binding energies, and magnetic moments of Fe clusters with 2 to 17 atoms. *Physical Review B* **2001**, *63*, DOI: 10.1103/physrevb.63.205407.

(18) Berwanger, J.; Polesya, S.; Mankovsky, S.; Ebert, H.; Giessibl, F. J. Atomically Resolved Chemical Reactivity of Small Fe Clusters. *Physical Review Letters* **2020**, *124*, DOI: 10.1103/physrevlett.124.096001.

View Article Online
DOI: 10.1039/D4NR02713B

(19) Ma, Q.-M.; Xie, Z.; Wang, J.; Liu, Y.; Li, Y.-C. Structures, binding energies and magnetic moments of small iron clusters: A study based on all-electron DFT. *Solid State Communications* **2007**, *142*, 114–119.

(20) Mpourmpakis, G.; Froudakis, G. E.; Andriotis, A. N.; Menon, M. Role of Co in enhancing the magnetism of small Fe clusters. *Physical Review B* **2005**, *72*, DOI: 10.1103/physrevb.72.104417.

(21) Guvelioglu, G. H.; Ma, P.; He, X.; Forrey, R. C.; Cheng, H. First principles studies on the growth of small Cu clusters and the dissociative chemisorption of<mml:math xmlns:mml="http://www.w3.org/1998/Math/MathML" display="inline"><mml:mrow><mml:msub><mml:mi mathvariant="normal">H</mml:mi><mml:mn>2</mml:mn><
Physical Review B **2006**, *73*, DOI: 10.1103/physrevb.73.155436.

(22) Montejo-Alvaro, F. et al. Icosahedral transition metal clusters (M13, M = Fe, Ni, and Cu) adsorbed on graphene quantum dots, a DFT study. *Physica E: Low-dimensional Systems and Nanostructures* **2019**, *110*, 52–58.

(23) Chen, Y.; Huang, Z.; Hu, P.; Chen, J.; Tang, X. Improved performance of supported single-atom catalysts via increased surface active sites. *Catalysis Communications* **2016**, *75*, 74–77.

(24) Wang, S. et al. Dopants adsorbed as single atoms prevent degradation of catalysts. *Nature Materials* **2004**, *3*, 143–146.

(25) Thomas, J. M.; Saghi, Z.; Gai, P. L. Can a Single Atom Serve as the Active Site in Some Heterogeneous Catalysts? *Topics in Catalysis* **2011**, *54*, 588–594.

(26) Zhu, Y. et al. Single-Atom Iron-Nitrogen Catalytic Site with Graphitic Nitrogen for Efficient Electroreduction of CO2. *ChemistrySelect* **2020**, *5*, 1282–1287.

(27) Lyu, D. et al. Ultra-high surface area graphitic Fe-N-C nanospheres with single-atom iron sites as highly efficient non-precious metal bifunctional catalysts towards oxygen redox reactions. *Journal of Catalysis* **2018**, *368*, 279–290.

(28) An, S. et al. High-Density Ultra-small Clusters and Single-Atom Fe Sites Embedded in Graphitic Carbon Nitride (g-C3N4) for Highly Efficient Catalytic Advanced Oxidation Processes. *ACS Nano* **2018**, *12*, PMID: 30183258, 9441–9450.

(29) Zhang, H. et al. A Graphene-Supported Single-Atom FeN5 Catalytic Site for Efficient Electrochemical CO2 Reduction. *Angewandte Chemie International Edition* **2019**, *58*, 14871–14876.

(30) Yang, X.-F. et al. Single-Atom Catalysts: A New Frontier in Heterogeneous Catalysis. *Accounts of Chemical Research* **2013**, *46*, PMID: 23815772, 1740–1748.

(31) Chen, Y.; Huang, Z.; Ma, Z.; Chen, J.; Tang, X. Fabrication, characterization, and stability of supported single-atom catalysts. *Catal. Sci. Technol.* **2017**, *7*, 4250–4258.

(32) Heiz, U.; Sanchez, A.; Abbet, S.; Schneider, W.-D. Catalytic Oxidation of Carbon Monoxide on Monodispersed Platinum Clusters: Each Atom Counts. *Journal of the American Chemical Society* **1999**, *121*, 3214–3217.

(33) Kaden, W. E.; Wu, T.; Kunkel, W. A.; Anderson, S. L. Electronic Structure Controls Reactivity of Size-Selected Pd Clusters Adsorbed on TiO2 Surfaces. *Science* **2009**, *326*, 826–829.

(34) Lei, Y. et al. Increased Silver Activity for Direct Propylene Epoxidation via Subnanometer Size Effects. *Science* **2010**, *328*, 224–228.

(35) Abbet, S. et al. Acetylene Cyclotrimerization on Supported Size-Selected Pdn Clusters ($1 < n < 30$): One Atom Is Enough! *Journal of the American Chemical Society* **2000**, *122*, 3453–3457.

(36) Haberland, H.; Karrais, M.; Mall, M.; Thurner, Y. Thin films from energetic cluster impact: A feasibility study. *Journal of Vacuum Science and Technology A: Vacuum, Surfaces, and Films* **1992**, *10*, 3266–3271.

(37) Gracia-Pinilla, M.; Martínez, E.; Vidaurri, G. S.; Pérez-Tijerina, E. Deposition of Size-Selected Cu Nanoparticles by Inert Gas Condensation. *Nanoscale Research Letters* **2009**, *5*, DOI: 10.1007/s11671-009-9462-z.

(38) Martínez-Carreón, M. J. et al. Synthesis and structural analysis of gold-palladium alloy nanoparticles using co-sputtering of independent sources. *Materials Research Express* **2019**, *6*, 046515.

(39) Silva, L. G. et al. Synthesis of Fe Nanoparticles Functionalized with Oleic Acid Synthesized by Inert Gas Condensation. *Journal of Nanomaterials* **2014**, *2014*, 1–6.

(40) Gracia-Pinilla, M.; Ferrer, D.; Mejía-Rosales, S.; Pérez-Tijerina, E. Size-Selected Ag Nanoparticles with Five-Fold Symmetry. *Nanoscale Research Letters* **2009**, *4*, DOI: 10.1007/s11671-009-9328-4.

(41) Pérez-Tijerina, E. et al. Highly size-controlled synthesis of Au/Pd nanoparticles by inert-gas condensation. *Faraday Discuss.* **2008**, *138*, 353–362.

View Article Online
DOI: 10.1039/D4NR02713B

(42) Chen, Y.; Huang, Z.; Ma, Z.; Chen, J.; Tang, X. Fabrication, characterization, and stability of supported single-atom catalysts. *Catalysis Science and Technology* **2017**, *7*, 4250–4258.

(43) Singh, B. et al. Single-Atom (Iron-Based) Catalysts: Synthesis and Applications. *Chemical Reviews* **2021**, *121*, 13620–13697.

(44) Takele Menisa, L. et al. Single atomic Fe–N4 active sites and neighboring graphitic nitrogen for efficient and stable electrochemical CO2 reduction. *Nanoscale Horizons* **2022**, *7*, 916–923.

(45) Zhu, Y. et al. Single-Atom Iron-Nitrogen Catalytic Site with Graphitic Nitrogen for Efficient Electroreduction of CO2. *ChemistrySelect* **2020**, *5*, 1282–1287.

(46) Lyu, D. et al. Ultra-high surface area graphitic Fe-N-C nanospheres with single-atom iron sites as highly efficient non-precious metal bifunctional catalysts towards oxygen redox reactions. *Journal of Catalysis* **2018**, *368*, 279–290.

(47) An, S. et al. High-Density Ultra-small Clusters and Single-Atom Fe Sites Embedded in Graphitic Carbon Nitride (g-C3N4) for Highly Efficient Catalytic Advanced Oxidation Processes. *ACS Nano* **2018**, *12*, 9441–9450.

(48) Zhang, H. et al. A Graphene-Supported Single-Atom FeN5 Catalytic Site for Efficient Electrochemical CO2 Reduction. *Angewandte Chemie International Edition* **2019**, *58*, 14871–14876.

(49) Shin, H.-J. et al. Control of Electronic Structure of Graphene by Various Dopants and Their Effects on a Nanogenerator. *Journal of the American Chemical Society* **2010**, *132*, 15603–15609.

(50) Kumar, B. et al. Controlled Growth of Semiconducting Nanowire, Nanowall, and Hybrid Nanostructures on Graphene for Piezoelectric Nanogenerators. *ACS Nano* **2011**, *5*, 4197–4204.

(51) Fernandez-Escamilla, H. N. et al. Understanding the Selectivity of the Oxygen Reduction Reaction at the Atomistic Level on Nitrogen-Doped Graphitic Carbon Materials. *Advanced Energy Materials* **2021**, *11*, 2002459.

(52) Alvarado-Leal, L. A. et al. Density Functional Theory Study of Single-Atom Transition Metal Catalysts Supported on Pyridine-Substituted Graphene Nanosheets for Oxygen Reduction Reaction. *ACS Applied Nano Materials* **2023**, *7*, 338–347.

(53) Habenicht, B. F.; Teng, D.; Semidey-Flecha, L.; Sholl, D. S.; Xu, Y. Adsorption and Diffusion of 4d and 5d Transition Metal Adatoms on Graphene/Ru(0001) and the Implications for Cluster Nucleation. *Topics in Catalysis* **2013**, *57*, 69–79.

(54) Barth, J. Transport of adsorbates at metal surfaces: from thermal migration to hot precursors. *Surface Science Reports* **2000**, *40*, 75–149.

(55) Han, B.; Li, F. Regulating the electrocatalytic performance for nitrogen reduction reaction by tuning the N contents in Fe3@NxC20-x (x = 0 4): a DFT exploration. *Journal of Materials Informatics* **2023**, *3*, DOI: 10.20517/jmi.2023.32.

(56) Geusic, M. E.; Morse, M. D.; Smalley, R. E. Hydrogen chemisorption on transition metal clusters. *The Journal of Chemical Physics* **1985**, *82*, 590–591.

(57) Yam, K.; Guo, N.; Jiang, Z.; Li, S.; Zhang, C. Graphene-Based Heterogeneous Catalysis: Role of Graphene. *Catalysts* **2020**, *10*, 53.

(58) Zhang, L.; Xu, Q.; Niu, J.; Xia, Z. Role of lattice defects in catalytic activities of graphene clusters for fuel cells. *Physical Chemistry Chemical Physics* **2015**, *17*, 16733–16743.

(59) Giannozzi, P. et al. QUANTUM ESPRESSO: a modular and open-source software project for quantum simulations of materials. *Journal of Physics: Condensed Matter* **2009**, *21*, 395502.

(60) Hohenberg, P.; Kohn, W. Inhomogeneous Electron Gas. *Phys. Rev.* **1964**, *136*, B864–B871.

(61) Kohn, W.; Sham, L. J. Self-Consistent Equations Including Exchange and Correlation Effects. *Phys. Rev.* **1965**, *140*, A1133–A1138.

(62) Perdew, J. P.; Burke, K.; Ernzerhof, M. Generalized Gradient Approximation Made Simple. *Phys. Rev. Lett.* **1996**, *77*, 3865–3868.

(63) Grimme, S.; Antony, J.; Ehrlich, S.; Krieg, H. A consistent and accurate ab initio parametrization of density functional dispersion correction (DFT-D) for the 94 elements H-Pu. *The Journal of Chemical Physics* **2010**, *132*, 154104.

(64) Monkhorst, H. J.; Pack, J. D. Special points for Brillouin-zone integrations. *Phys. Rev. B* **1976**, *13*, 5188–5192.

View Article Online
DOI: 10.1039/D4NR02713B

(65) Novoselov, K. S. et al. Electric Field Effect in Atomically Thin Carbon Films. *Science* **2004**, *306*, 666–669.

(66) Henkelman, G.; Arnaldsson, A.; Jónsson, H. A fast and robust algorithm for Bader decomposition of charge density. *Computational Materials Science* **2006**, *36*, 354–360.

(67) Yu, M.; Trinkle, D. R. Accurate and efficient algorithm for Bader charge integration. *The Journal of Chemical Physics* **2011**, *134*, DOI: 10.1063/1.3553716.

(68) Jin, C. et al. Adsorption of Transition-Metal Clusters on Graphene and N-Doped Graphene: A DFT Study. *Langmuir* **2022**, *38*, PMID: 35285652, 3694–3710.

View Article Online
DOI: 10.1039/D4NR02713B

Data Availability Statement

The data supporting this article have been included as part of the Supplementary Information. Any further details please do not hesitate contacting us. (jmromo@ens.cnyn.unam.mx or luis.alvaradoll@uanl.edu.mx)

Exploring Nitrogen-Mediated Effects on Fe and Cu Cluster Development in Graphene: A DFT Study.

L. A. Alvarado-Leal, J. I. Páez-Ornelas, M. A. Ruiz-Robles, J. Guerrero-Sánchez, J. M. Romo-Herrera, H. N. Fernández-Escamilla, Noboru Takeuchi, E.G. Perez-Tijerina.